Understanding Tribocorrosion of Aluminum at the Crystal Level

Kaiwen Wang, Zhengyu Zhang, Raja Shekar B. Dandu, and Wenjun Cai*

Department of Materials Science and Engineering, Virginia Polytechnic Institute and State University, Blacksburg, VA 24060, USA

*Corresponding author's E-mail addresses: caiw@vt.edu (W. Cai)

Abstract

Aluminum (Al) and its alloys are excellent corrosion-resistant materials due to their sustained passivity in neutral aqueous solutions. However, tribocorrosion remains a major threat to the integrity of Al, during which corrosion and wear work synergistically to accelerate material degradation. In this work, a combined experimental and computational investigation was carried out using Al single crystals to develop a crystal-based tribocorrosion modeling framework that accounts for the effects of lattice reorientation and dislocations on surface corrosion. Specifically, the mechanical, corrosion, and tribocorrosion properties of Al (100), (110), and (111) single crystals were measured experimentally, followed by characterization of lattice rotation and dislocation density via electron backscattered diffraction (EBSD). Unlike the mechanical and corrosion properties that are orientation-dependent, the tribocorrosion rate was found to be insensitive to the initial orientations of the crystals. Using the experimental results as inputs and validations, a multiphysics finite element model was developed that successfully predicted the depassivation and repassivation currents during tribocorrosion by mapping the local corrosion kinetics as a function of passivation state, crystallographic orientation, and dislocation density. It was found that lattice rotation, rather than dislocations, dominates the overall tribocorrosion behavior. Finally, the decrease of orientation-dependence during tribocorrosion was explained in terms of the coupling between the un-rotated lattice in the unworn region and the rotated lattice from the worn region.

Keywords: tribology; corrosion, aluminum, EBSD, finite element analysis

1. Introduction

Aluminum (Al) and its alloys are widely used passive metals for applications that require lightweight and corrosion-resistant materials, including marine, transportation, aerospace industries, coastal infrastructures, and energy devices, etc. [1-6] Pure Al, along with its alloys, benefit from a naturally formed dense oxide layer which protects the metal from further corrosion [7, 8]. However, in complex service conditions, what jeopardizes the longevity of the Al-based structure is more often tribocorrosion, namely the synergistic material degradation caused by wear and corrosion [2, 9-11]. The mechanical damage during wear often leads to significantly increased corrosion rate for Al due to the depassivation on the wear track, and the coupling between the passivated and depassivated surface regions with different Volta potentials [12, 13]. Thus, understanding the tribocorrosion behavior and mechanism of Al is extremely important from both fundamental and practical points of view.

Theories and analytical models have been developed based on experimental observations to account for the localized, wear-accelerated corrosion for passive metals such as Al, Ti, stainless steel, and CoCrMo alloys [14-18], which are well summarized in several recent papers [18, 19]. For example, Olsson et al. [17] developed an analytical solution to model the current transients during reciprocal tribocorrosion of CoCrMo alloys in a series of electrolytes by accounting for both the confined mechanical contact geometry, and interface-limited passive film growth at the interface. Policastro et al. [18] measured and modeled the wear-assisted corrosion current of super-duplex stainless steel after tribocorrosion in 0.6 M NaCl electrolyte from a single-asperity contact model. They found that by accounting for the stress in the interfacial film growth, an Arrhenius-type relationship could be established between the wear-assisted corrosion current and the peak Hertzian contact stress. Based on experimental results on Al 7075-T6 alloys, Li et al. [20] proposed that the accelerated corrosion for samples under tribocorrosion is due to the coupling between the depassivated worn region and the passive unworn region. In another research carried out on stainless steel, Chen et al. [21] found that the phase transformation induced by plastic deformation will lead to accelerated corrosion. So far, the developed tribocorrosion models often consider the metals to have isotropic mechanical and electrochemical properties, without considering their crystal alignment and the associated anisotropy [11, 17, 22].

In addition to experimental investigations and analytical models, a few attempts have been made to build numerical models to understand stressed corrosion and tribocorrosion using finite element (FE) method [13, 19, 23, 24]. Cheng [25] proposed a stress corrosion model to explain the shift in equilibrium potential due to the increase in dislocation density induced by plastic strain based on theories developed

by Gutman [26]. FE models were built based on this model and successfully accounted for the localized accelerated corrosion in plastically deformed areas of stainless steel pipelines [23, 24]. Recently, we developed an experimentally-validated FE simulation framework to predict tribocorrosion rate maps for Al alloys as a function of their mechanical and electrochemical properties [13]. In this model, the depassivation/repassivation effect and potential shift due to plastic strain were considered to predict the mechanical and chemical wear rates during tribocorrosion.

However, none of the prior studies considers tribocorrosion at the crystal level, where anisotropy could arise from different crystal alignment, wear-induced lattice reorientation and dislocation generation. Yet, most properties of metals are sensitive to anisotropy [27-29]. Indeed, both experimental and computational studies have confirmed the anisotropy in mechanical and electrochemical behavior for single crystal and polycrystal metal surfaces with different crystal orientations [30-34]. For example, <111> textured Al7075 composite was found to exhibit higher wear resistance than its non-textured counterparts [35]. Using molecular dynamics simulations, Komanduri et al. studied the anisotropy in hardness and friction of single crystal Al with various crystal orientations [36, 37]. Liu et al. predicted the difference in load-displacement curves, pile-up patterns, and lattice rotation angles of Al using crystal plasticity FE model [38]. On the other hand, for electrochemical behavior, Yasuda et al. [39], Treacy et al. [40] and Davis et al. [41] reported differences in the open circuit potentials, pitting potentials, and metastable pitting frequencies of single crystal Al samples with different surface orientations. Li et al. [42] showed that (200) textured Al-Mg alloy fabricated via selective laser melting exhibited better corrosion resistance than its non-textured cast counterparts.

Inspired by the well-known crystal plasticity models, the goal of this work is to combine tribocorrosion experiments, materials characterization, and multiphysics FE simulations to develop a numerical modeling framework for tribocorrosion of passive metals using single crystal Al as model material. Specifically, micro-indentation and electrochemical tests were carried out to characterize the mechanical and electrochemical properties of single crystal Al samples with (100), (110) and (111) surface planes. A linear interpolation method proven by the research by Bland et al. [43] and Barrett et al. [44] was used to interpolate electrochemical properties of a given crystal orientation based on the measured results of (100), (110) and (111) samples. After the tribocorrosion tests, EBSD characterization of the tribocorroded surfaces was performed to measure the local lattice reorientation and dislocation density as model inputs. Finally, a multiphysics FE model was developed and validated, which accurately predicted

the wear-induced corrosion current evolution during tribocorrosion by considering the local passivation state, lattice reorientation, and subsurface dislocations, following the schematic shown in **Fig. 1(a)**.

2. Experimental Methods

2.1. Material, mechanical, electrochemical, and tribocrrosion testing

(100), (110), and (111) single crystal pure Al samples of >99.99% purity and 10×10×0.5 mm^3 size was obtained from MTI Corp, CA. Micro-indentation tests were carried out using a multifunctional tribometer (Rtec MFT-5000, CA) with a conical diamond tip with a half angle of 30° and 12.5 micron radius, as shown in **Fig. 1(b)**. A trapezoidal loading function with 0.1 N max load, and 0.005 N/sec loading and unloading rates was used for micro-indentation tests for all samples.

The potentiodynamic (PD) polarization tests of all samples were carried out in a three-electrode setup using a Gamry 600 potentiostat/galvanostat/ZRA in neutral 0.6 M NaCl aqueous solution at room temperature. An exposed area of 1 cm^2 of the sample was used as the working electrode (WE). The counter electrode (CE) and the reference electrode (RE) were the mixed metal oxide coated Ti mesh and 1 M KCl Ag/AgCl electrode respectively. After a stabilization step of 5 min at the open circuit potential (OCP), the PD tests were conducted from -1.7 to -0.2 V vs. RE. The transfer coefficient α were calculated from Tafel slope β using $\alpha = \frac{2.303 k_B T}{e\beta}$, where k_B is the Boltzmann's constant ($1.380649 \times 10^{-23}\, J \cdot K^{-1}$), T is the absolute temperature (293.15 K) and e is the charge of an electron ($1.602 \times 10^{-19} C$). The corrosion potential (E_{corr}), corrosion current density (i_{corr}), anodic and cathodic transfer coefficient (α_a and α_c) were obtained using Tafel extrapolation method from the polarization curves at ±100 mV above and below OCP. It is noted that deviation of Tafel behavior was observed in the cathodic branch at potentials more negative than – 1.45 V vs. RE, likely due to the diffusion controlled cathodic behavior of O_2 reduction, as well as in the anodic branch, likely due to the growth of the passive layer when Al is anodized. Thus, fitting anodic and cathodic transfer coefficient (α_a and α_c) at potentials much higher or lower than the OCP may lead to inaccurate kinetics parameters. The validity of the parameters fitted under this practice is later proved by the comparation between the PD curves simulated by the FE method and those measured experimentally (see Fig. 9(a)).

The tribocorrosion tests of all samples were carried out using a multifunctional tribometer (Rtec MFT-5000, CA) with a 12.5 micron conical diamond indenter in neutral 0.6 M NaCl aqueous solution at room temperature, as shown in **Fig. 1 (c)**. To ensure that all samples reach a uniform, stable electrochemical state prior to the tribocorrosion test, all the samples were anodized at a constant potential

of -1 V vs. the RE for 3 hours before the test. A single-stroke scratching test was carried out at 0.1 mm/s speed over 2 mm scratch length for each sample. The same anodic potential (-1 V vs. RE) was applied to the sample during the whole scratching process. The tribocorrosion current evolution was recorded as a function of scratching time and compared with the simulation results afterwards. The selection of a hard micro-indenter tip and a single stroke wear mode, instead of flat-on-flat reciprocal wear modes allows the easy capture of wear contact area and temporal evolution of surface corrosion current. All reported tests were repeated for 2-4 times.

2.2. Materials characterization

Electron backscattered diffraction (EBSD) characterization was carried out on the tribocorroded samples using a FEI Helios 600 FIB microscope at 20 kV and 1.4 nA. The cross-sectional samples (in the ND-TD plane, as defined in **Fig. 1(c)**) were prepared by mechanical polishing with SiC sandpaper down to 1200 grits, followed by fine polishing using alumina suspension of 1 µm, 0.3 µm and 0.05 µm. A final step of vibratory polishing was carried out using the Buehler Vibromet2 polisher with 0.02 µm colloidal silica suspension to remove the residual stress induced by mechanical polishing. EBSD orientation maps of 140 × 113 µm^2 were acquired at step size of 200 nm. The dislocation density was calculated from the EBSD results using the MTEX package [45], based on the method proposed by Pantleon [46], which correlates the dislocation density tensor with the curvature of the crystalline lattice using Nye's tensor as [47] $\alpha_{ik} = \kappa_{ki} - \delta_{ki}\kappa_{mm}$, where α_{ik} denotes the ik component of the dislocation density tensor, κ_{ki} denotes the *ki* component of the lattice curvature tensor, δ_{ki} is the Kronecker delta function. κ_{mm} is the sum of the three diagonal components $\kappa_{mm} = \kappa_{11} + \kappa_{22} + \kappa_{33}$. It's worth noting that the 2D cross-sectional EBSD data lacks information along SD, which is assumed to be negligible in this work due to the similar loading conditions for every cross-sectional plane along SD. Thus, the value for dislocation density is considered to be only slightly underestimated using this method. The initial dislocation density (N_0) of the as-received samples was obtained by averaging the dislocation density from areas far away from the wear track (~ 80 - 100 µm below the surface).

3. Multiphysics FE models

A 2D FE model was developed using the COMSOL Multiphysics software of version 5.3 on the ND-TD plane of the sample (i.e. normal to SD). **Fig. 1(a)** summarizes the integration of experiments and FE simulations. Specifically, experimentally measured wear track geometry, EBSD maps, and dislocation

density maps were used as inputs of the FE model, while the measured tribocorrosion current evolution as model validation, as detailed next. Three factors were considered to account for the localized, accelerated corrosion in the vicinity of the wear track: (1) change of local corrosion potential and current density due to the deformation-induced change of surface crystal orientations, (2) change of corrosion potential due to the increase in dislocation density, and (3) loss of corrosion protection due to depassivation in the wear track.

3.1. Geometry and meshing

Fig. 2 summarizes the model geometry and meshing before ($t < t_s$), during ($t_s < t < t_f$), and after ($t > t_f$) tribocorrosion tests, where t_s and t_f represents the starting and finishing time respectively. For the electrochemical test, as well as tribocorrosion test prior to scratching ($t < t_s$), a 2D model with rectangular sample geometry was built, as shown in **Fig. 2 (a)**. A uniform meshing size of 7.5 μm was assigned for both the electrolyte and Al sample (WE). During tribocorrosion, the sample geometry was taken from the EBSD measurements, as shown in **Fig. 2 (b)**, with coarser meshing size (7.5 μm) for regions far away and finer meshing size (with a minimum size of 0.025 μm) near the wear track. The total worn area was calculated by multiplying the cross-sectional area by the scratching distance, which increased with scratching time. After the scratching was finished ($t > t_f$), the whole wear track (over the entire scratch length) was assumed to be passive again, where the repassivation kinetics was governed by the oxide growth on the wear track, as described next.

3.2. Governing equations and boundary conditions for electrochemical test

To model the PD test, the applied potential between the WE and CE was swept between -1.6 and -0.8 V with a step size of 0.1 V. In the cathodic branch of the PD curve, the corrosion reaction kinetics on Al surface was assumed to follow the Butler-Volmer equation:

$$i_{B-V} = i_{corr}\left(exp\left(\frac{\alpha_a F\eta}{RT}\right) - exp\left(\frac{\alpha_c F\eta}{RT}\right)\right), \quad (1)$$

where i_{corr} stands for the equilibrium corrosion current density, α_a and α_c stands for the anodic and cathodic transfer coefficient respectively. η is for the overpotential, which could be expressed as

$$\eta = E_{app} - E_{el} - E_{corr}, \quad (2)$$

where E_{app} is the applied potential, E_{el} is the potential drop in the electrolyte and E_{corr} is the corrosion potential obtained from the experiment.

During anodic polarization, Al is oxidized into Al_2O_3, forming a passive layer at the surface. In this work, it is assumed that the Al current density decreases as the thickness of passive layer increases due to its higher electrical resistance than that of Al. The passive layer will form at a rate according to Faraday's laws:

$$v_n = \frac{i_{B-V}M}{nF\rho}, \tag{3}$$

where *M* is the molar mass of aluminum oxide, *n=3* is the number of electrons transferred in forming one Al_2O_3 molecule, *F* is the Faraday's constant (96485 C/mol), and ρ is the density of the aluminum oxide. The thickness of the oxide *s* was then calculated based on this growth rate as

$$s(t) = \int_o^t v_n(t)dt = \frac{M}{nF\rho}\int_o^t i_{B-V}(t)dt. \tag{4}$$

The electrical resistance of aluminum oxide was used to account for the passivation effect of the entire surface. The conductivity of the aluminum oxide σ was taken as $1 \times 10^{-12} S/m$. In this case, the Butler-Volmer equation is still valid, but the current blocking effect of the passive layer needs to be considered. Thus, the overpotential η in the anodic region was further modified by the potential drop on the oxide film as

$$\eta = E_{app} - E_{el} - E_{corr} - i_{B-V}(t)\frac{s(t)}{\sigma}. \tag{5}$$

The Butler-Volmer current and oxide thickness from the previous time step was used to calculate the overpotential in eq. (5), which was then used to predict the Butler-Volmer current of the new time step. The final Butler-Volmer current density was predicted with 1 min passivation time at a time step of 1s for each applied potential step to account for the growth of the passive layer during the measurement of PD curve. This assumption is later proven to capture the feature of the PD curve of the samples including its passive behavior successfully.

3.3. Governing equations and boundary conditions for tribocorrosion test

The simulation of tribocorrosion was realized by coupling the electrochemical kinetics with crystal orientation and dislocation density effects, as shown in the **Fig. 2 (d)**. First, the effect of crystal orientation on local electrochemical properties, including corrosion potential and corrosion current density, was implemented through linear interpolation from the experimental data of three representative orientations using a self-developed MATLAB code. By solving (E_0, E_1, E_2) from the following equation set,

$$\begin{cases} E_0 + E_1\, tan(\theta_{(001)}/2)\, cos\, \Phi_{(001)} + E_2\, tan(\theta_{(001)}/2)\, sin\, \Phi_{(001)} = E_{corr(001)} \\ E_0 + E_1\, tan(\theta_{(011)}/2)\, cos\, \Phi_{(011)} + E_2\, tan(\theta_{(011)}/2)\, sin\, \Phi_{(011)} = E_{corr(011)} \\ E_0 + E_1\, tan(\theta_{(111)}/2)\, cos\, \Phi_{(111)} + E_2\, tan(\theta_{(111)}/2)\, sin\, \Phi_{(111)} = E_{corr(111)} \end{cases} \quad (7)$$

the corrosion potential of a random orientation (hkl) was obtained as

$$E_{corr(hkl)} = E_0 + E_1\, tan(\theta_{(hkl)}/2)\, cos\, \Phi_{(hkl)} + E_2\, tan(\theta_{(hkl)}/2)\, sin\, \Phi_{(hkl)}. \quad (8)$$

The same interpolation method was also applied to obtain corrosion current density i_{corr} for a given (hkl) plane. Using the interpolated E_{corr} and i_{corr}, local values of E_{corr} and i_{corr} were calculated based on the crystal orientation obtained from EBSD. Because the EBSD data is in the form of a hexagonal grid with 200 nm step size while the meshing for the FE model is a triangular meshing with step size ranging from 25 nm to 7.5 µm, the maps for E_{corr} and i_{corr} were smoothed with piecewise cubic method between adjacent EBSD data points and the interpolated data was then used in the FE model.

It is also noted here that the use of the interpolation method was motivated by previous experimental [48] and modeling studies [49], which found that corrosion rate follows a smooth transition between adjacent orientations. This assumption is further supported by our preliminary results on a low symmetry orientation (Fig. S4 in Supplemental Materials). Nonetheless, the linear interpolation could be an over-simplification of the problem and a more precise determination of the corrosion potential and current density could be developed either with more data points of the low symmetrical orientations or more physics-based inputs of this model. This is left for future study.

The effect of dislocation density on electrochemical thermodynamics and kinetics was implemented using the theory developed by Gutman [26, 50]. It assumes that the increase in dislocation density caused by wear will increase the active corrosion site, resulting in a drop in the corrosion potential following [23, 26]:

$$E_{corr}{}' = E_{\text{corr}} - \frac{\sigma_y V_m}{nF} - \frac{RT}{nF} \ln\left(\frac{N}{N_0}\right) \quad (9)$$

The second term denotes the drop in corrosion potential for the deformation within the elastic limit, where σ_y is the yield strength, V_m is the molar volume of aluminum ($V_m = 9.99 \times 10^{-6} m^3/mol$), n is the electron involved in the reaction (n=3). For materials going through plastic deformation, which will cause the dislocation density in the sample to increase from N_0 to N, the potential will be further reduced as expressed in the third term, where T is temperature (T=298 K at room temperature), R is the ideal gas constant (R=8.3145J/(mol · K)), and F is the Faraday's constant (96485 C/mol). The readers are referred to Eqn 23 of Ref [26] for the original derivation of this equation.

During tribocorrosion, the worn area was defined to be depassivated, and the rest of the surface remained passive. For the passive region, a 4.5 nm thick oxide was assigned, which was taken from the average of the measured aluminum oxide thickness (3.8~5.1 nm) on Al in NaCl solution reported by Natishan et al. [51]. Inside the depassivated wear region, starting from the highest point to the bottom of the wear track, the oxide thickness was assigned an initial value of zero, which were then allowed to grow according to eq. (3) and (4) during subsequent tribocorrosion test, to model the repassivation of wear tracks after the indenter has passed away. The same oxide-growth repassivation kinetics was applied for the sample after the tribocorrosion test.

4. Results and discussions

4.1. Mechanical and corrosion properties of Al single crystals

Fig. 3(a) shows the micro-indentation test results of all samples. A difference in the maximum displacement could be observed, with (111) sample possessing the lowest indentation depth of ~ 6.33 μm, indicating it is the hardest orientation, while (100) sample is the softest with a maximum depth of ~ 7.00 μm. This result agrees with the hardness ranking indicated by previous experiments from Liu et al. [38]. The maximum displacement for (111) sample is 10.6% larger than that for (100) sample. Using the mechanical properties of different surface orientations (as listed in **Table 1** from references [36, 38]), the load-displacement curve was also simulated using the FE method, which matched well with the experimental results. The detailed modeling information could be found in **Figs. S1** and **S2** of the supplementary materials. **Fig. 3(b)** plots the PD curves of all samples, reflecting their differences in electrochemical properties, The measured corrosion potential (E_{corr}), corrosion current density (i_{corr}), anodic and cathodic transfer coefficients are listed in **Table 2**. These parameters indicate that the overall corrosion resistance could be ranked as (111) > (110) > (100) sample. Such trend agrees well with several prior reports [39, 40].

4.2. Tribocorrosion behavior

Fig. 4(a) shows the tribocorrosion results of (111) sample under different normal loads of 0.1 – 0.7 N. A sudden surge of the corrosion current could be observed at the beginning of the scratching, which were found to increase with scratching time, likely due to increased depassivated/worn area. The peak current, as well as the repassivation time after the finish of the test, was found to increase with the applied load. Such load-dependence is consistent with the results of several previous models [18, 19]. **Fig. 4(b)**

demonstrates the current evolution during tribocorrosion test under the same 0.3 N load for different samples. It could be seen that even though the performance for pure wear (estimated from hardness ranking obtained by indentation test) and pure corrosion follows the ranking: (100) < (110) < (111), the tribocorrosion performance reflected by the current increase of the three samples are similar. This experimental finding proves once again that the tribocorrosion material loss is not a simple summation of pure wear and corrosion. The reason for such similar tribocorrosion current will be explained later in Section 4.4.

4.3. Subsurface characterization of tribocorroded samples

Figs. 5-7 shows the EBSD results of the tribocorroded (100), (110) and (111) samples under 0.3 N load. A V-shaped wear trench was observed for all samples, confirming the single-asperity contact from the indenter geometry. SEM images in Figs. 5-7(a) shows that the scratch depth from the base of the wear track to the original surface of (100), (110) and (111) sample is around 15.8 μm, 15.3 μm and 14.0 μm respectively, consistent with the ranking of their indentation hardness. The wear track width at the height of the original surface of (100), (110) and (111) sample is about 13.5 μm, 13.0 μm, and 10.5 μm respectively. The product of the scratch depth, width, and a constant scratch length, indicates that the wear volume also follows the same ranking. In addition to material removal, significant lattice rotation (i.e. reorientation) has been observed, similar to those reported in bronze after dry sliding wear [52]. During pin-on-disc dry sliding wear, the grains were found to be sheared in the sliding direction (SD) with rotation axis around the transverse direction (TD) of the pin [52]. In the present study, for the harder (111) sample, the lattice rotation direction was rather similar from both sides of the V-shaped wear track in the SD-orientation map (**Fig. 7(c)**), indicating a shear-induced lattice rotation along SD direction. On the other hand, ND- and TD-orientation maps (**Fig. 7(b) and (d)**) show lattice rotation in the opposite direction, similar to the lattice rotation field predicted by the crystal plasticity finite element model [53]. Such trend was less apparent in the softer (100) and (110) samples, as shown in **Figs. 5 and 6**, where lattice rotations around all three directions can be observed. This is likely related to the formation of higher amounts of pile-up in these softer materials, which alters the local shear deformation along SD (hence lattice rotation around TD axis) with additional lattice rotation around SD axis (i.e. pile-up flow direction).

The dislocation density in the samples after tribocorrosion test was obtained using these EBSD data, as plotted in **Fig. 8**. An increase in the dislocation density could be observed at the region near the wear track. The initial dislocation density N_0 for (100), (110) and (111) samples are $7.9 \times 10^{13}, 7.2 \times$

10^{14} and $7.7 \times 10^{13}\ m^{-2}$ respectively, which increased to $\sim 10^{15}\ m^{-2}$ after tribocorrosion. This behavior is similar to the dislocation density change observed in nanocrystalline Al under wear [54].

4.4. Tribocorrosion simulation results

Prior to the tribocorrosion simulation, electrochemical behavior of the samples was simulated within the Tafel-range, as shown in **Fig. 9(a)**, based on the experimental parameters in **Table 2**. It can be seen that the simulated results agree well with the experimental measurements, proving the effectiveness of the electrochemical kinetics setup in the model, as well as the input parameters for (100), (110) and (111) samples. Using the interpolation method introduced in eq. (7) and (8) and the electrochemical parameters obtained for (100), (110) and (111) samples, the interpolated E_{corr} and i_{corr} map for any arbitrary orientation was generated and shown in **Fig. 9 (b) and (c)**. The anodic and cathodic transfer coefficient was not interpolated because the variance was negligible. Combining the interpolated E_{corr} and i_{corr} with the EBSD data, maps of local E_{corr} and i_{corr} for the deformed samples were obtained, as plotted in **Fig. 10**. After considering the dislocation density effect using eq. (3), $E_{corr}{}'$ is plotted in **Fig. 11**. The resulting current density distribution in the electrolyte for the tribocorrosion system is also plotted in **Fig. 11**, showing higher current density in the vicinity of the wear track.

The simulated surface current distribution along the x-axis (TD) at time t_s, corresponding to the state where the indenter has just depassivated the surface, is plotted in **Fig. 12**. Three sets of current density were calculated to demonstrate the different roles of initial lattice orientation, crystal reorientation and dislocation density. **Fig. 12(a)** is the result predicted by only including the crystallographic interpolated electrochemical parameters and the wear track depassivation effect, without considering the dislocation effect. Higher current density could be observed near the wear track. However, the current of (100) near the wear track is significantly lower than that of (110) and (111). This is because the lattice rotation caused by wear raises the corrosion potential and lowers the corrosion current density near the wear track for (100) samples, which could be inferred from **Fig. 11**. Thus, even though the wear track is depassivated, the increase in local current density is small. While in the case of (110) and (111) samples, both crystallographic effect and depassivation effect would increase the current density near the wear track. **Fig. 12(b)** is the surface corrosion current predicted by only including the dislocation effect, without considering the crystallographic effect or wear track depassivation effect. It can be seen that the (100) sample demonstrates slightly more significant coupling caused by dislocation than the other two samples. **Fig. 12(c)** considers all three effects. With all the effects considered, the three samples reach a similar

overall current density level. For all samples, the highest current density is always at the edge of the wear track.

To validate the effectiveness of the model with different assumptions, the total interface current during the tribocorrosion process was calculated using the integration method discussed below. As shown in **Fig. 2**, the total current of the wear track could be interpreted as the integration of the current at different location of the wear track. At time *t*, the indenter has been scratching for time $t - t_s$ and is thus at position $v(t - t_s)$ along the SD, where v is the velocity of the indenter. The wear track area right underneath the indenter is in a completely depassivated state while the starting point has been repassivated for time $t - t_s$. The area in between has a repassivation time which changes linearly from 0 to $t - t_s$. Thus, assume the total interface current for the 2D model is $i(T)$ (converted to the unit of nA/mm) when repassivation has taken place for time T, the total current for the whole wear track (when indenter has been moving) for time T is

$$I(t) = \mathrm{v}\int_0^{t-\mathrm{t_s}} i(T)dT. \tag{9}$$

After time t_f, the repassivation time along the wear track is a slow transition from $t - t_f$ at the end of the wear track to $t - t_s$ at the beginning of the wear track. Thus, the total current will be

$$I(t) = v\int_{t-t_f}^{t-t_s} i(T)dT. \tag{10}$$

The result of the temporal evolution of current density and oxide thickness as a function of position of the (100) sample is shown in **Fig. 13** as an example. As shown in **Fig 13(a)**, the oxide thickness distribution along the x-axis (TD) changes with time as the surface repassivates. The repassivation rate inside the wear track (x = 50 -70 μm) is faster than that outside the wear track (x < 50 μm). The oxide thickness changes at the bottom of the wear track with respect to the repassivation time is plotted in **Fig 13(b)**. Repassivation happens at a fast rate at the beginning and slows down as the oxide film grows thicker. At T = 100 s (i.e. $t = t_f$), the passive layer inside the wear track grows to a thickness of around 1.8 nm. This could be translated to an oxide thickness distribution along the y-axis (SD), as show in **Fig. 13(c)**. At $t = t_f$, the end of the wear track is completely depassivated while the beginning of the wear track has an oxide thickness that has been repassivated for 20 s. The 2D interface current $i(T)$ corresponding to repassivation time T is plotted in **Fig. 13(d)**, where the total current $I(t)$ is integrated using $i(T)$ based on eqns. (9) and (10).

The total current predicted by only considering the crystallographic effect and depassivation effect is plotted in **Fig. 14(a-c)**. The current predicted under this assumption is clearly below the experimental

results, especially for (100) sample. Even though the coupling between different orientations and depassivated areas causes the total current to increase during the tribocorrosion, these two effects are not enough to account for all the current increase. Only after considering the dislocation effect, a good match between the simulation and experimental results is achieved for the total tribocorrosion current, as shown in **Fig. 14(d-f)**.

Similar to the experimental results, the simulated tribocorrosion behavior of the three samples are similar, even though (100) sample has the lowest strength and the worst corrosion resistance. The simulation results presented above could explain this phenomenon. Comparing the current peak in **Fig. 14(a) and Fig. 14(d)** for (100) sample, dislocation-induced coupling between the worn and unworn areas were found to contribute to a significant fraction of the overall wear-induced corrosion current rise. This is much different from the cases of (110) and (111) samples, in which crystal orientation and depassivation effect almost accounts for all the current increase. Just as discussed in section 4.3, in the case of (110) and (111) samples, the lattice reorientation contributes significantly to the coupling between the wear track and unworn region. On the other hand, for the (100) sample, the crystal orientation inside the wear track changes from (100) to other orientations, so that the coupling between the wear track and unworn region is reduced. This brings the tribocorrosion current of the (100) sample down to the same level as (110) and (111) samples.

4.5. Discussions

Lastly, several limitations of this modeling framework are discussed briefly, which requires future research. First, the extrapolation of corrosion current density using Tafel extrapolation should be practiced with care. In cases where a clear linear domain (at least one decade) in the log scale is absent from the PD curves, corrosion current density cannot be obtained from Tafel extrapolation. In such cases, alternative corrosion rate measurements from weight loss, surface height change, potentiostatic and electrochemical impedance tests could be implemented.

Second, the assumption and usage of the linear intercept method in determining the corrosion current and potential of low symmetry orientations from those of the high symmetry orientations (see Section 3.3 for details) need further validation. Prior research on the effects of crystallographic anisotropy on corrosion is limited, especially those for low symmetry orientations. For example, Lindell and Pettersson [48] showed that in 316L stainless steel, the corrosion rate increased in the order (111)<(110)≈(100), indeed similar to the trend observed in this study for pure Al, both of which are passive

metals. In addition, by combining EBSD and confocal laser microscopy, effects of crystallographic anisotropy on corrosion was studied in 18 orientations, covering a wide orientation space (see Fig. 7 in Ref. [48]). These orientations not only include the high symmetry orientations, such as (111), (110), and (100), but also various lower symmetry orientations, such as (157), (456), (367), and (458) (see Table 2 in Ref. [48] for the complete hkl index for all orientations). It was found that the corrosion rate of lower symmetry orientations lies within the values of the high symmetry orientations. As a comparison, the corrosion current density calculated using the linear interpolation method in this study (Fig. 9) agrees qualitatively well with these experimental observations in steel.

In terms of the crystallographic effects of Al single crystals and alloys, there is still a large discrepancy among the literature reports so far, which are likely due to the high sensitivity of corrosion behavior not only to crystal orientation, but also the composition [55], aging condition [4], and even surface treatment techniques [56]. For example, Wen et al. found that in single crystal Al-2 wt%Cu alloys, the corrosion rate increased in the order of (111) < (001) < (101) in the solid solution alloys. After aging and precipitation of the θ' phases, corrosion current density increased in the order of (111) > (001) > (101), where the (111) orientation changes from the most corrosion resistant to the most susceptible orientation, due to different substrate strain resulting from the precipitation. Yasuda et al. [57] studied the corrosion behavior of Al and Al-Cu with up to 4.2 wt % Cu, and discovered that in terms of pitting potential E_{pit}, (100) > (110) > (111), in agreement with our study.

To evaluate whether the corrosion behavior of a random low symmetry orientation of Al single crystal indeed falls within a reasonable range of that predicted using the linear intercept method, additional experiments were performed, as shown in the **Supplemental Materials Section 2.2**. A low symmetry (i.e. high hkl index) orientation was prepared from Al single crystal, whose orientation index was determined to be (921) by orientation mapping and inverse pole figure (IPF), as shown in Fig. S4(b) and (c) respectively. The Euler angle of this sample is around (358.4°, 85.5°, 70.3°). The PD results shows that its cathodic reaction kinetics is not linear, hence a Tafel extrapolation of corrosion current is not possible. Nonetheless, the pitting corrosion of (921) is similar to that of (110), and both the cathodic and anodic branch of its PD curve lies in between (100) and (110) orientations, which are indeed the two close by orientations in the IPF. Based on these preliminary results, we believe that the prediction using the linear intercept method is a good approximation. Nonetheless, the above observations do not rule out the possibility that there could be orientations don't obey this rule. More low symmetry orientations should be studied to cover a wider range of the orientation space to further evaluate this hypothesis in the future.

Lastly, it is worth pointing out that the tribocorrosion test in this work is a single pass scratch using a sharp conical tip. This process doesn't result in a nanocrystalline layer at the surface as observed in some previous works [58-60], which use the ball-on-disk setup for multiple passes. The more severe plastic deformation during the multiple-pass wear might lead to more significant change in the electrochemical status due to the grain size effect and denser dislocations [8, 61, 62]. This question would be a future field of interest for advancing the current model.

5. Conclusions

In this work, the crystallographic effects on the tribocorrosion behavior of single crystal Al in 0.6 M NaCl aqueous solution was investigated using both experiments and FE simulations. The micro-indentation and PD test confirmed the orientation-dependent mechanical and electrochemical properties for (100), (110), and (111) Al samples. Based on the experimental inputs, a multiphysics FE model was developed to study tribocorrosion at the crystal level. The model included the depassivation-repassivation effect, the orientation-dependent electrochemical properties, and the change in equilibrium corrosion potential caused by dislocation density. The results from the integrated experimental and simulation study lead to the following conclusions:

(1) From experimental results, it could be indicated that the wear resistance and corrosion resistance of the (100) Al sample is the worst and (111) is the best. For hardness, (100) < (110) < (111). For open circuit potential, (100) < (110) < (111). For corrosion current density, (100) > (110) > (111).

(2) From the simulation results, it could be concluded that the maximum corrosion current is located near the edge of the wear track. The depassivation-repassivation effect, crystallographic effect and dislocation effect all plays an important role in the localized, accelerated corrosion in the tribocorrosion process, among which, the impacts of lattice reorientation are more significant than that of dislocations.

(3) The strong orientation-dependence diminished during tribocorrosion because the crystallographic effect reduces the coupling between the worn region and unworn region for (100) sample, while increases the coupling in the case of (110) and (111).

The success in this single crystal tribocorrosion model has great significance in helping to explain the underlying mechanisms of tribocorrosion. It could be adapted in the future to simulate other material systems or act as a first step to build models with more complex microstructures or testing conditions.

Acknowledgement

The authors gratefully acknowledge funding provided by US National Science Foundation (DMR-1856196, 2104655). This work was performed in part at the Nanoscale Characterization and Fabrication Laboratory, which is supported by the Virginia Tech National Center for Earth and Environmental Nanotechnology Infrastructure (NanoEarth), a member of the National Nanotechnology Coordinated Infrastructure (NNCI), supported by NSF (ECCS 1542100 and ECCS 2025151). The computational resource used in this work is provided by the advanced research computing (ARC) at Virginia Polytechnic Institute and State University. Z.Z. and R.D. sincerely thank Dr. Jonathan Angle at VT NCFL for assisting the sample preparation and EBSD characterization.

References

[1] A.C. Vieira, L.A. Rocha, N. Papageorgiou, S. Mischler, Mechanical and electrochemical deterioration mechanisms in the tribocorrosion of Al alloys in NaCl and in NaNO3 solutions, Corros Sci 54 (2012) 26-35.
[2] H. Mraied, W.J. Cai, The effects of Mn concentration on the tribocorrosion resistance of Al-Mn alloys, Wear 380-381 (2017) 191-202.
[3] J. Chen, J.W. Xiao, C.Y. Hung, W.B. Wang, J. Zhao, F.M. Michel, C. Deng, W.J. Cai, Effects of alloying concentration on the aqueous corrosion and passivation of aluminum-manganese-molybdenum concentrated alloys , Corros Sci 198 (2022).
[4] F. Wen, J.Q. Chen, S.B. Zhong, Z.X. Zhou, S. Han, H.G. Wei, Y.H. Zhang, W.R. Li, R.G. Guan, Effect of crystal orientations and precipitates on the corrosion behavior of the Al-Cu alloy using single crystals, J Alloy Compd 890 (2022).
[5] K.D. Ralston, N. Birbilis, M. Weyland, C.R. Hutchinson, The effect of precipitate size on the yield strength-pitting corrosion correlation in Al-Cu-Mg alloys, Acta Mater 58(18) (2010) 5941-5948.
[6] Y.K. Zhu, J.D. Poplawsky, S.R. Li, R.R. Unocic, L.G. Bland, C.D. Taylor, J.S. Locke, E.A. Marquis, G.S. Frankel, Localized corrosion at nm-scale hardening precipitates in Al-Cu-Li alloys, Acta Mater 189 (2020) 204-213.
[7] D.D. Macdonald, Passivity - the key to our metals-based civilization, Pure Appl Chem 71(6) (1999) 951-978.
[8] H. Mraied, W.J. Cai, A.A. Sagues, Corrosion resistance of Al and Al-Mn thin films, Thin Solid Films 615 (2016) 391-401.
[9] S. Mischler, S. Debaud, D. Landolt, Wear-accelerated corrosion of passive metals in tribocorrosion systems, J Electrochem Soc 145(3) (1998) 750-758.
[10] S. Mischler, A. Spiegel, D. Landolt, The role of passive oxide films on the degradation of steel in tribocorrosion systems, Wear 225 (1999) 1078-1087.
[11] D. Landolt, S. Mischler, M. Stemp, Electrochemical methods in tribocorrosion: a critical appraisal, Electrochim Acta 46(24-25) (2001) 3913-3929.
[12] W.B. Wang, K.W. Wang, Z.Y. Zhang, J. Chen, T.Y. Mou, F.M. Michel, H.L. Xin, W.J. Cai, Ultrahigh tribocorrosion resistance of metals enabled by nano-layering, Acta Mater 206 (2021).
[13] K.W. Wang, Y.N. Wang, X.W. Yue, W.J. Cai, Multiphysics modeling and uncertainty quantification of tribocorrosion in aluminum alloys, Corros Sci 178 (2021).
[14] N. Papageorgiou, S. Mischler, Electrochemical Simulation of the Current and Potential Response in Sliding Tribocorrosion, Tribol Lett 48(3) (2012) 271-283.

[15] S.F. Cao, S.G. Maldonado, S. Mischler, Tribocorrosion of passive metals in the mixed lubrication regime: theoretical model and application to metal-on-metal artificial hip joints, Wear 324 (2015) 55-63.
[16] J. Chen, J.W. Xiao, J. Poplawsky, F.M. Michel, C. Deng, W.J. Cai, The origin of passivity in aluminum-manganese solid solutions, Corros Sci 173 (2020).
[17] C.O.A. Olsson, A.N.I. Munoz, S.F. Cao, S. Mischler, Modeling Current Transients in a Reciprocal Motion Tribocorrosion Experiment, J Electrochem Soc 168(3) (2021).
[18] S.A. Policastro, J.M. Shockley, M.J. Strom, C.R. So, D.J. Horton, K.J. Wahl, Predicting the corrosion-wear response of an isolated austenite phase under anodic polarization, Wear 494-495 (2022).
[19] S.F. Cao, S. Mischler, Modeling tribocorrosion of passive metals - A review, Curr Opin Solid St M 22(4) (2018) 127-141.
[20] Z.Y. Li, H.Y. Yu, D.B. Sun, The tribocorrosion mechanism of aluminum alloy 7075-T6 in the deep ocean, Corros Sci 183 (2021).
[21] X. Chen, M. Gussev, M. Balonis, M. Bauchy, G. Sant, Emergence of micro-galvanic corrosion in plastically deformed austenitic stainless steels, Mater Design 203 (2021).
[22] P. Jemmely, S. Mischler, D. Landolt, Electrochemical modeling of passivation phenomena in tribocorrosion, Wear 237(1) (2000) 63-76.
[23] L.Y. Xu, F. Cheng, A finite element based model for prediction of corrosion defect growth on pipelines, Int J Pres Ves Pip 153 (2017) 70-79.
[24] Z. Zhu, P.J. Teevens, H. Xue, F.Y. Cheng, Numerical Simulation and Experimental Verification of Pitting Corrosion Propagation in Sweet Pipeline Service, Journal of Pipeline Science and Engineering (2022).
[25] Y.F. Cheng, Stress corrosion cracking of pipelines, John Wiley & Sons2013.
[26] E.M. Gutman, Thermodynamics of the mechanico-chemical effect - II. the range of operation of nonlinear laws, Soviet Materials Science 3(4) (1967) 293-297.
[27] A. Brahme, J. Fridy, H. Weiland, A.D. Rollett, Modeling texture evolution during recrystallization in aluminum, Model Simul Mater Sc 17(1) (2009).
[28] H.R. Wenk, P. Van Houtte, Texture and anisotropy, Rep Prog Phys 67(8) (2004) 1367-1428.
[29] J.S. Kallend, U.F. Kocks, A.D. Rollett, H.R. Wenk, Operational Texture Analysis, Mat Sci Eng a-Struct 132 (1991) 1-11.
[30] A. Shahryari, J.A. Szpunar, S. Orrianovic, The influence of crystallographic orientation distribution on 316LVM stainless steel pitting behavior, Corros Sci 51(3) (2009) 677-682.
[31] K. Hagihara, M. Okubo, M. Yamasaki, T. Nakano, Crystal-orientation-dependent corrosion behaviour of single crystals of a pure Mg and Mg-Al and Mg-Cu solid solutions, Corros Sci 109 (2016) 68-85.
[32] G.L. Song, Z.Q. Xu, Crystal orientation and electrochemical corrosion of polycrystalline Mg, Corros Sci 63 (2012) 100-112.
[33] J.M. Song, Y.S. Zou, C.C. Kuo, S.C. Lin, Orientation dependence of the electrochemical corrosion properties of electrodeposited Cu foils, Corros Sci 74 (2013) 223-231.
[34] E.O. Fanijo, J.G. Thomas, Y. Zhu, W. Cai, A.S. Brand, Surface Characterization Techniques: A Systematic Review of their Principles, Applications, and Perspectives in Corrosion Studies, J Electrochem Soc 169(11) (2022).
[35] V. Chakkravarthy, S. Jerome, Fabrication of preferentially oriented Al4043 alloy and its wear anisotropy, Mater Lett 280 (2020).
[36] R. Komanduri, N. Chandrasekaran, L.M. Raff, MD simulation of indentation and scratching of single crystal aluminum, Wear 240(1-2) (2000) 113-143.
[37] R. Komanduri, N. Chandrasekaran, L.M. Raff, MD Simulation of nanometric cutting of single crystal aluminum-effect of crystal orientation and direction of cutting, Wear 242(1-2) (2000) 60-88.
[38] M. Liu, C. Lu, K.A. Tieu, C.T. Peng, C. Kong, A combined experimental-numerical approach for determining mechanical properties of aluminum subjects to nanoindentation, Sci Rep-Uk 5 (2015).
[39] M. Yasuda, F. Weinberg, D. Tromans, Pitting Corrosion of Al and Al-Cu Single-Crystals, Journal of the Electrochemical Society 137(12) (1990) 3708-3715.

[40] G.M. Treacy, C.B. Breslin, Electrochemical studies on single-crystal aluminium surfaces, Electrochimica Acta 43(12-13) (1998) 1715-1720.
[41] B.W. Davis, P.J. Moran, P.M. Natishan, Metastable pitting behavior of aluminum single crystals, Corros Sci 42(12) (2000) 2187-2192.
[42] R.D. Li, M.B. Wang, T.C. Yuan, B. Song, C. Chen, K.C. Zhou, P. Cao, Selective laser melting of a novel Sc and Zr modified Al-6.2 Mg alloy: Processing, microstructure, and properties, Powder Technol 319 (2017) 117-128.
[43] L.G. Bland, K. Gusieva, J.R. Scully, Effect of Crystallographic Orientation on the Corrosion of Magnesium: Comparison of Film Forming and Bare Crystal Facets using Electrochemical Impedance and Raman Spectroscopy, Electrochim Acta 227 (2017) 136-151.
[44] T.J. Barrett, A. Eghtesad, R.J. McCabe, B. Clausen, D.W. Brown, S.C. Vogel, M. Knezevic, A generalized spherical harmonics-based procedure for the interpolation of partial datasets of orientation distributions to enable crystal mechanics-based simulations, Materialia 6 (2019) 100328.
[45] R. Hielscher, H. Schaeben, A novel pole figure inversion method: specification of the MTEX algorithm, J Appl Crystallogr 41 (2008) 1024-1037.
[46] W. Pantleon, Resolving the geometrically necessary dislocation content by conventional electron backscattering diffraction, Scripta Mater 58(11) (2008) 994-997.
[47] J.F. Nye, Some Geometrical Relations in Dislocated Crystals, Acta Metall Mater 1(2) (1953) 153-162.
[48] D. Lindell, R. Pettersson, Crystallographic effects in corrosion of austenitic stainless steel 316L, Mater Corros 66(8) (2015) 727-732.
[49] S. Sahu, G.S. Frankel, Phase Field Modeling of Crystallographic Corrosion Pits, J Electrochem Soc 169(2) (2022).
[50] E.m.M. Gutman, Mechanochemistry of solid surfaces, World Scientific, Singapore ; River Edge, NJ, 1994.
[51] P.M. Natishan, W.E. O'Grady, Chloride Ion Interactions with Oxide-Covered Aluminum Leading to Pitting Corrosion: A Review, J Electrochem Soc 161(9) (2014) C421-C432.
[52] W. Cai, P. Bellon, A.J. Beaudoin, Probing the subsurface lattice rotation dynamics in bronze after sliding wear, Scripta Mater 172 (2019) 6-11.
[53] A. Kareer, E. Tarleton, C. Hardie, S.V. Hainsworth, A.J. Wilkinson, Scratching the surface: Elastic rotations beneath nanoscratch and nanoindentation tests, Acta Mater 200 (2020) 116-126.
[54] Y.Q. Shi, I. Szlufarska, Wear-induced microstructural evolution of nanocrystalline aluminum and the role of zirconium dopants, Acta Materialia 200 (2020) 432-441.
[55] M. Yasuda, F. Weinberg, D. Tromans, Pitting Corrosion of Al and Al‐Cu Single Crystals, Journal of The Electrochemical Society (137) (1990) 3708.
[56] K.P. Sherif, R. Narayan, Electrochemical behaviour of aluminium in 1M NaCl solution: Part 1: Open circuit potential measurements, British Corrosion Journal 24(3) (1989) 199.
[57] M. Yasud, F. Weinberg, D. Tromans, Pitting Corrosion of AI and AI-Cu Single Crystals, J Electrochem Soc 137(12) (1990) 3708-3715.
[58] R. Buscher, G. Tager, W. Dudzinski, B. Gleising, M.A. Wimmer, A. Fischer, Subsurface microstructure of metal-on-metal hip joints and its relationship to wear particle generation, J Biomed Mater Res B 72b(1) (2005) 206-214.
[59] A. Emge, S. Karthikeyan, D.A. Rigney, The effects of sliding velocity and sliding time on nanocrystalline tribolayer development and properties in copper, Wear 267(1-4) (2009) 562-567.
[60] J. Stojadinovic, D. Bouvet, M. Declercq, S. Mischler, Effect of electrode potential on the tribocorrosion of tungsten, Tribol Int 42(4) (2009) 575-583.
[61] S. Gollapudi, Grain size distribution effects on the corrosion behaviour of materials, Corros Sci 62 (2012) 90-94.
[62] K.D. Ralston, D. Fabijanic, N. Birbilis, Effect of grain size on corrosion of high purity aluminium, Electrochim Acta 56(4) (2011) 1729-1736.

Tables and Figures

Table 1. Mechanical properties of the (100), (110) and (111) Al used in this work.

Al crystal / Mechanical Properties	(100)	(110)	(111)	Ref
E (GPa)	63.7	72.6	76.1	[36]
σ_y (MPa)	61.39	61.63	63.12	[38]

Table 2. Electrochemical properties of the (100), (110) and (111) samples obtained from experimentally measured polarization curves, where E_{corr}, i_{corr}, and α_c and α_a represents the corrosion potential, corrosion current, and the cathodic and anodic transfer coefficient respectively.

Al crystal / Corrosion Properties	(100)	(110)	(111)
E_{corr} (V vs. Ag/AgCl)	-1.39 ± 0.011	-1.36 ± 0.036	-1.34 ± 0.010
i_{corr} ($\times 10^{-4} mA/cm^2$)	3.83 ± 1.04	1.65 ± 0.34	0.44 ± 0.085
α_c	0.49 ± 0.0025	0.49 ± 0.011	0.48 ±0.0068
α_a	0.24 ± 0.050	0.23 ± 0.023	0.24 ± 0.022

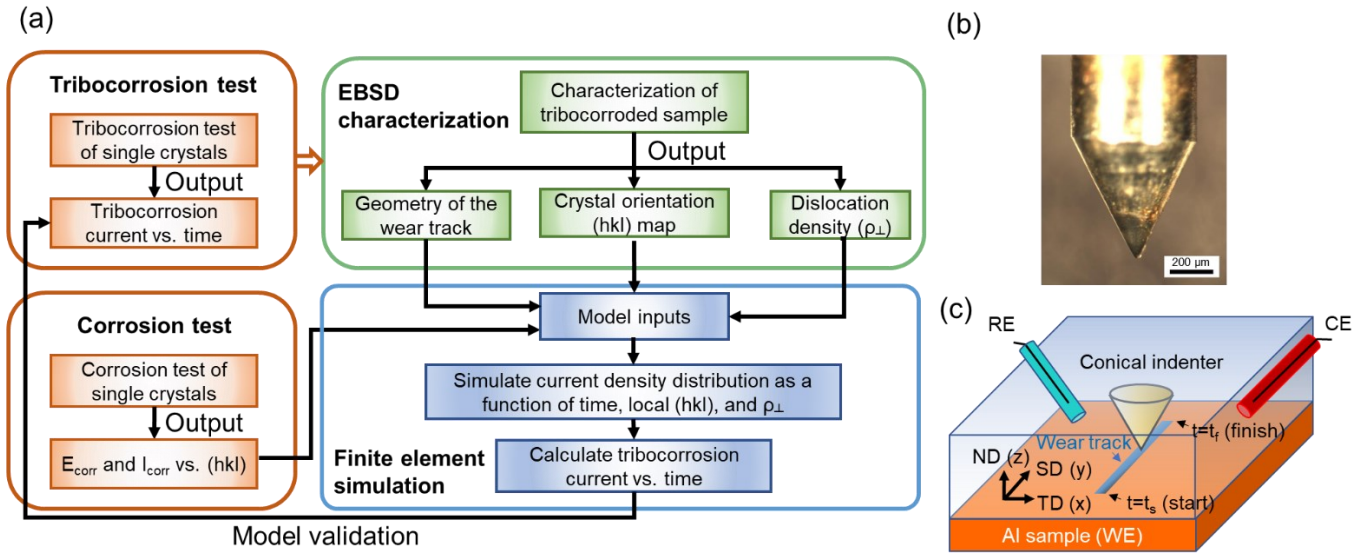

Figure 1. (a) Flowchart of the experiment and FE simulation integration, including experimental data acquisition, analysis, simulation, and model validation steps. (b) Optical microscopic image of the conical tip used for the micro-indentation and tribocorrosion experiments, and (c) schematic of the tribocorrosion test, where ND, SD, TD represents the normal, scratching, and transverse direction respectively.

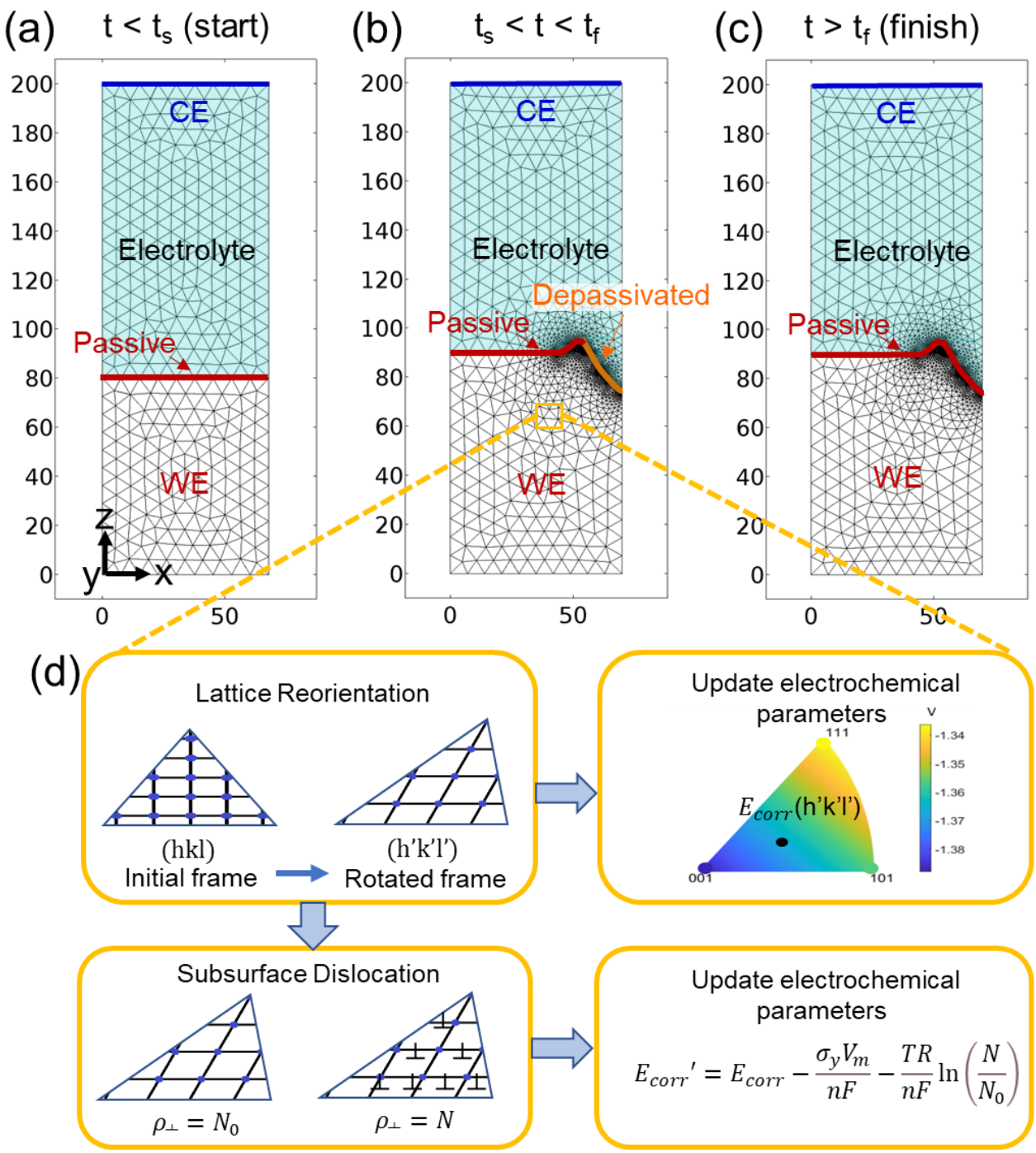

Figure 2. Summary of the FE tribocorrosion model setup and geometry (a) before ($t \leq t_s$), (b) during ($t_s < t < t_f$), and (c) after ($t \geq t_f$) the tribocorrosion test, where t_s and t_f represents the starting and finishing time respectively. (d) Schematic of the local electrochemical parameter (e.g. E_{corr}) mapping as a function of the lattice reorientation and dislocation density.

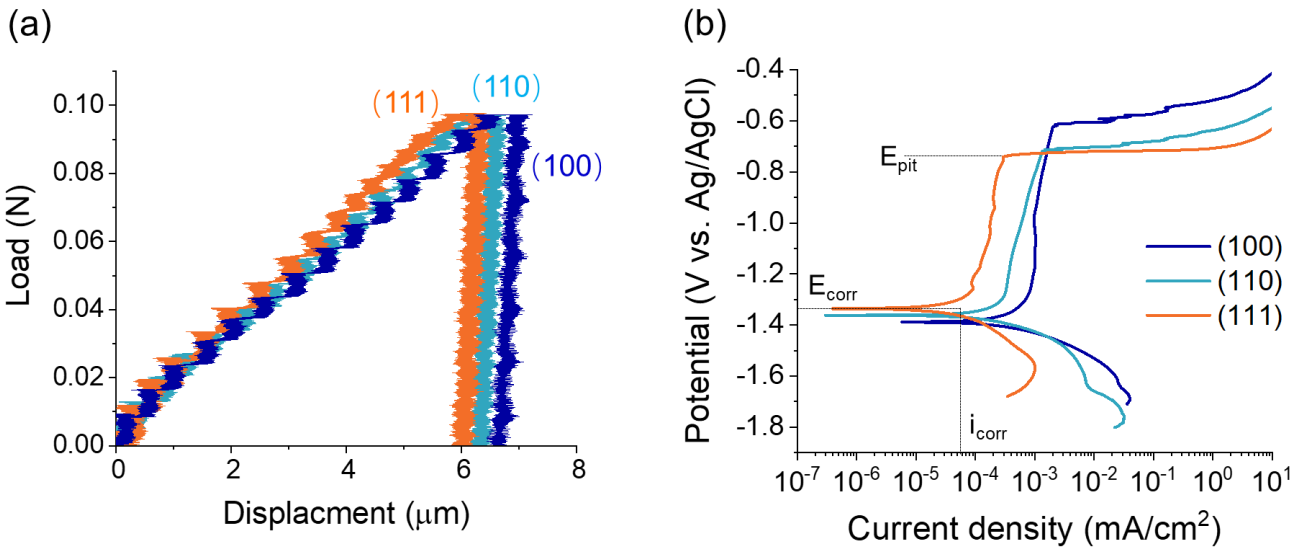

Figure 3. Experimentally measured (a) load-displacement curves from dry micro-indentation test, and (b) potentiodynamic polarization curves of (100), (110), and (111) Al single crystal samples in 0.6 M NaCl aqueous solution.

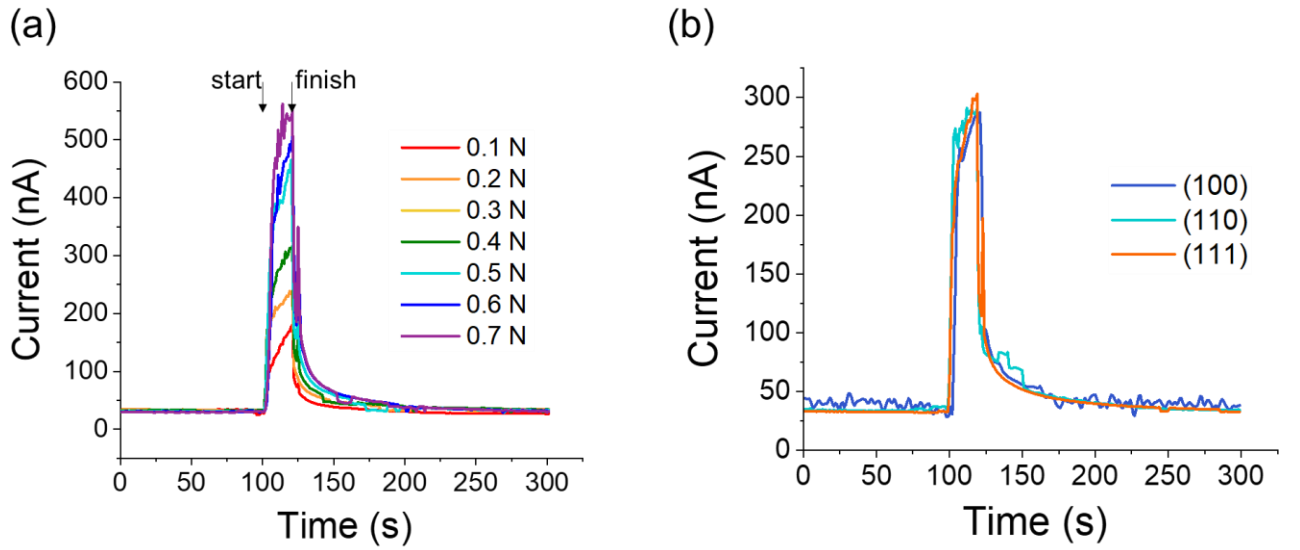

Figure 4. Tribocorrosion experiment results: (a) Temporal evolution of corrosion current of (111) Al sample during tribocorrosion test under different loads of 0.1 – 0.7 N. (b) Corrosion current evolution of all samples during tribocorrosion under 0.3 N normal load.

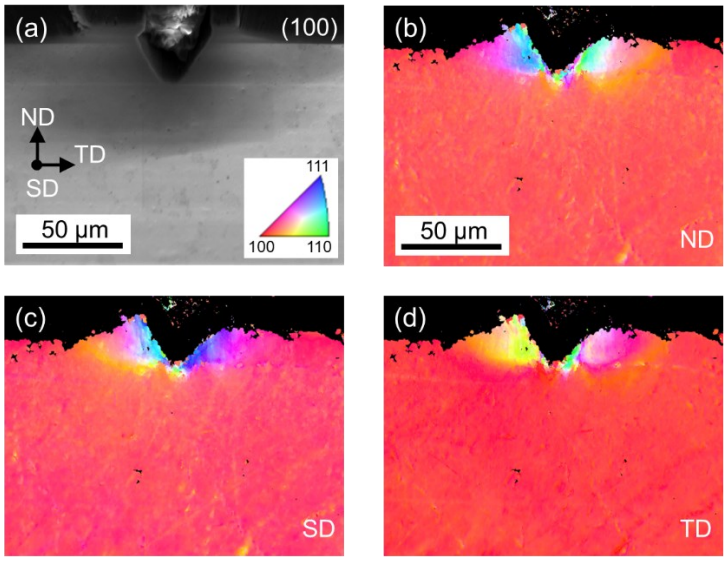

Figure 5. (a) SEM image and (b-d) corresponding EBSD maps of (100) Al cross-sectional sample after tribocorrosion test under 0.3 N. Images (b), (c), and (d) are plotted with orientations in the ND, SD, TD directions respectively, as defined in Fig. 1(b). All EBSD maps are color coded per the triangle legend in (a).

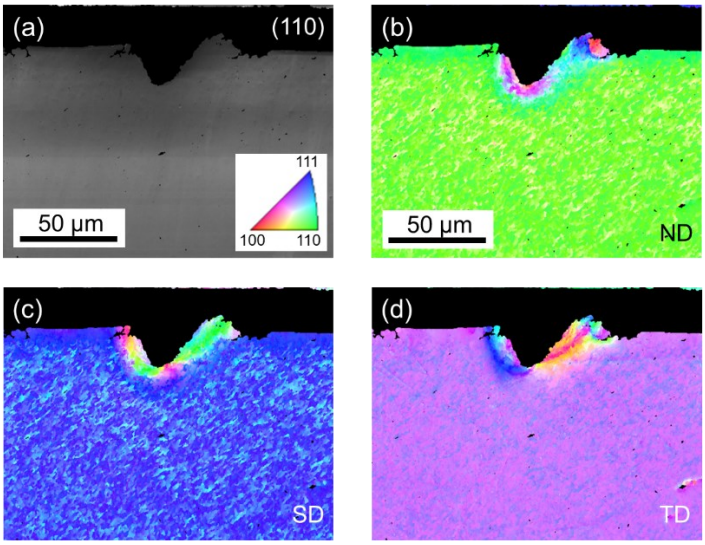

Figure 6. (a) SEM image and (b-d) corresponding EBSD maps of (110) Al cross-sectional sample after tribocorrosion test under 0.3 N. Images (b), (c), and (d) are plotted with orientations in the ND, SD, TD directions respectively, as defined in Fig. 1(b). All EBSD maps are color coded per the triangle legend in (a).

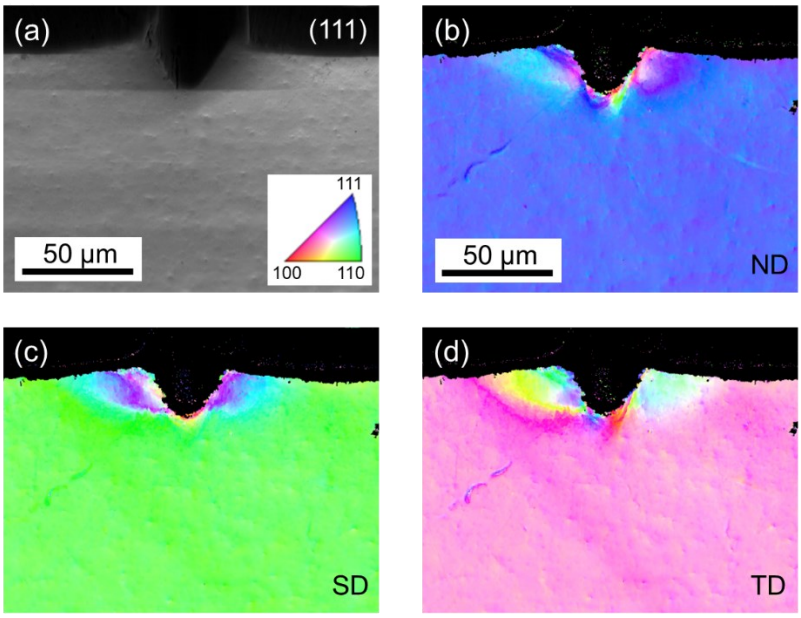

Figure 7. (a) SEM image and (b-d) corresponding EBSD maps of (111) Al cross-sectional sample after tribocorrosion test under 0.3 N. Images (b), (c), and (d) are plotted with orientations in the ND, SD, TD directions respectively, as defined in Fig. 1(b). All EBSD maps are color coded per the triangle legend in (a).

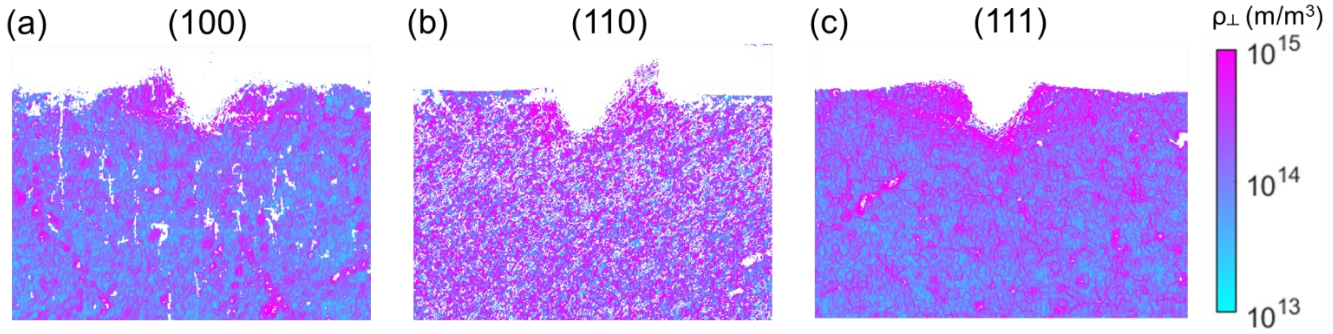

Figure 8. Calculated dislocation density maps of (a) (100), (b) (110), and (c) (111) tribocorroded sample obtained from EBSD results shown in Figs. 5-7.

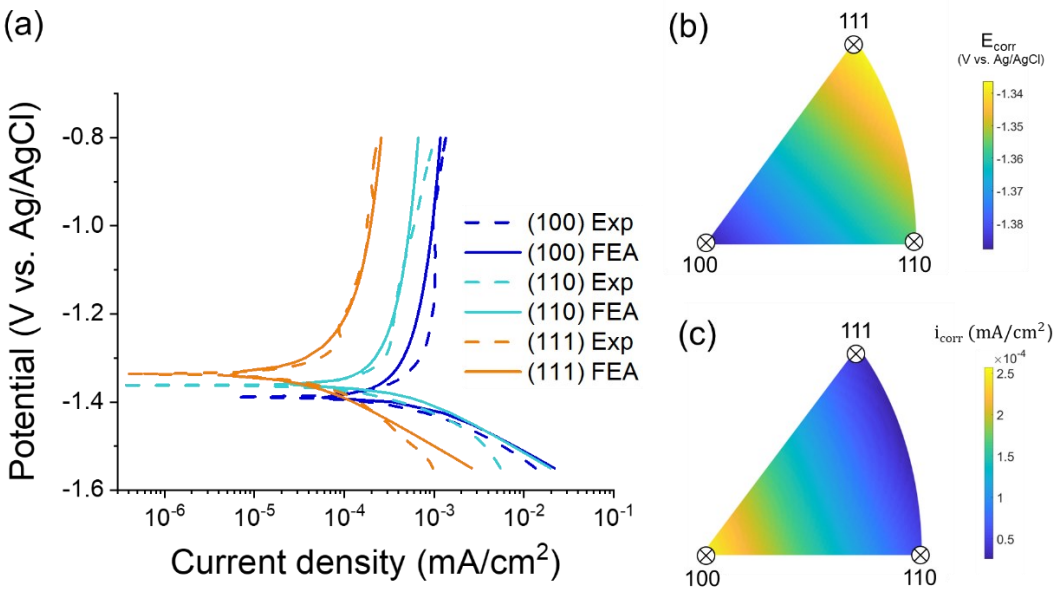

Figure 9. (a) Potentiodynamic polarization curves of all samples predicted by FE indentation simulation in comparison with experiments. (b) Interpolated corrosion potential and (c) corrosion current density map as a function of crystal orientations. Cross marks in (b) and (c) corresponds to experimental measurements, while the rest were interpolated per algorithm detailed in Section 3.

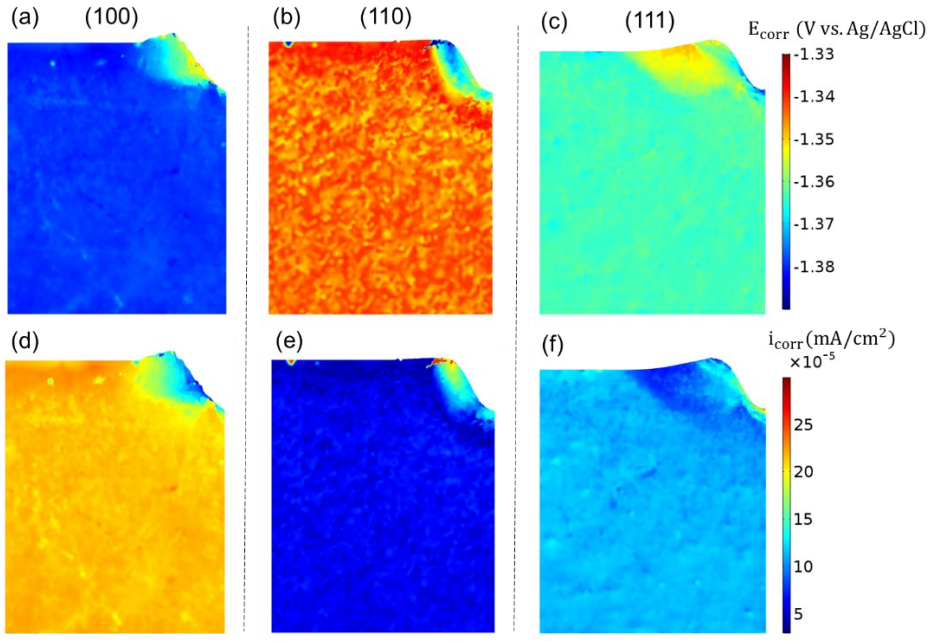

Figure 10. (a-c) Interpolated corrosion potential (E_{corr}) and (d-f) corrosion current density (i_{corr}) of tribocorroded surfaces of (100), (110), and (111) samples per corrosion maps developed in Figs. 9(b-c).

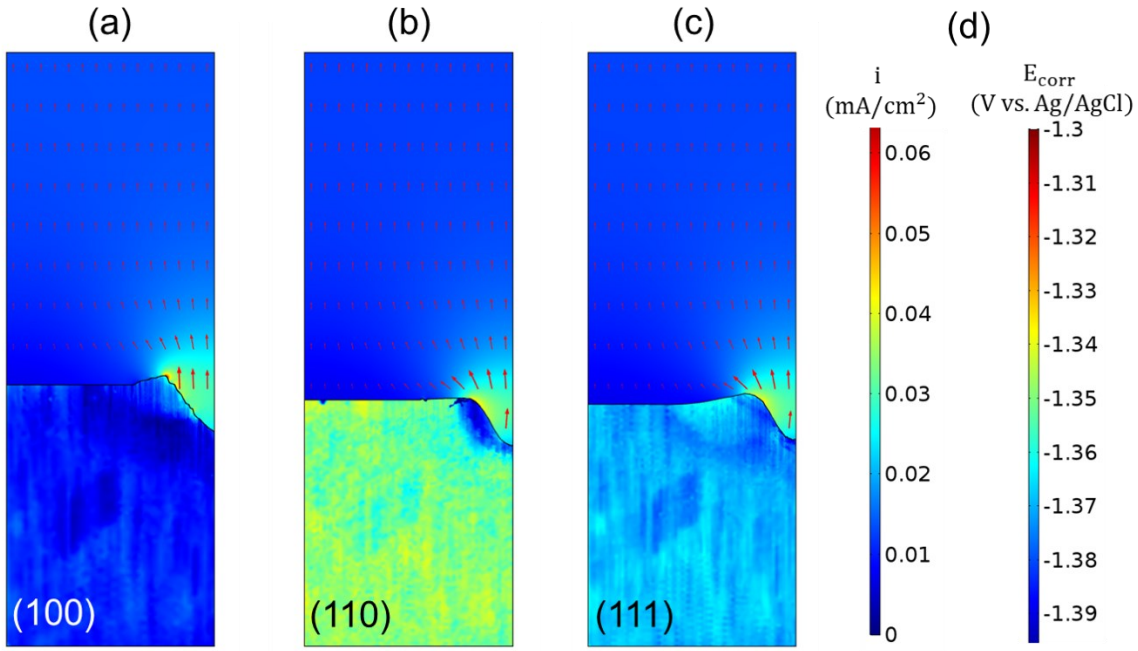

Figure 11. FE simulated current density within the electrolyte (i) and corrosion potential (E_{corr}) distribution of (a) (100), (b) (110), and (c) (111) samples during tribocorrosion. The FE model considers both lattice reorientation and subsurface dislocation density effects per algorithms detailed in Section 3.1.

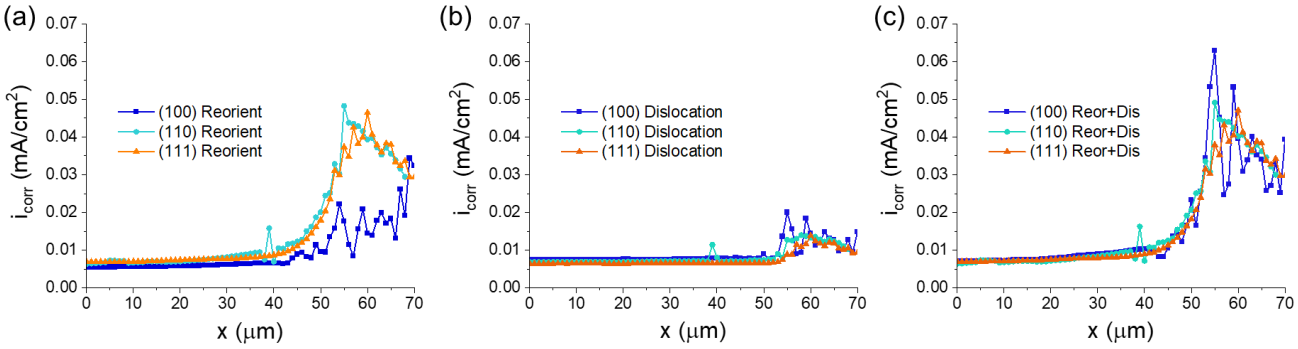

Figure 12. FE simulated current density distribution along the surface direction (defined in Fig. 2, where x=70 μm corresponds to the center of the wear track) during tribocorrosion considering (a) only lattice reorientation effect, (b) only dislocation effect, and (c) both lattice reorientation and subsurface dislocation effects.

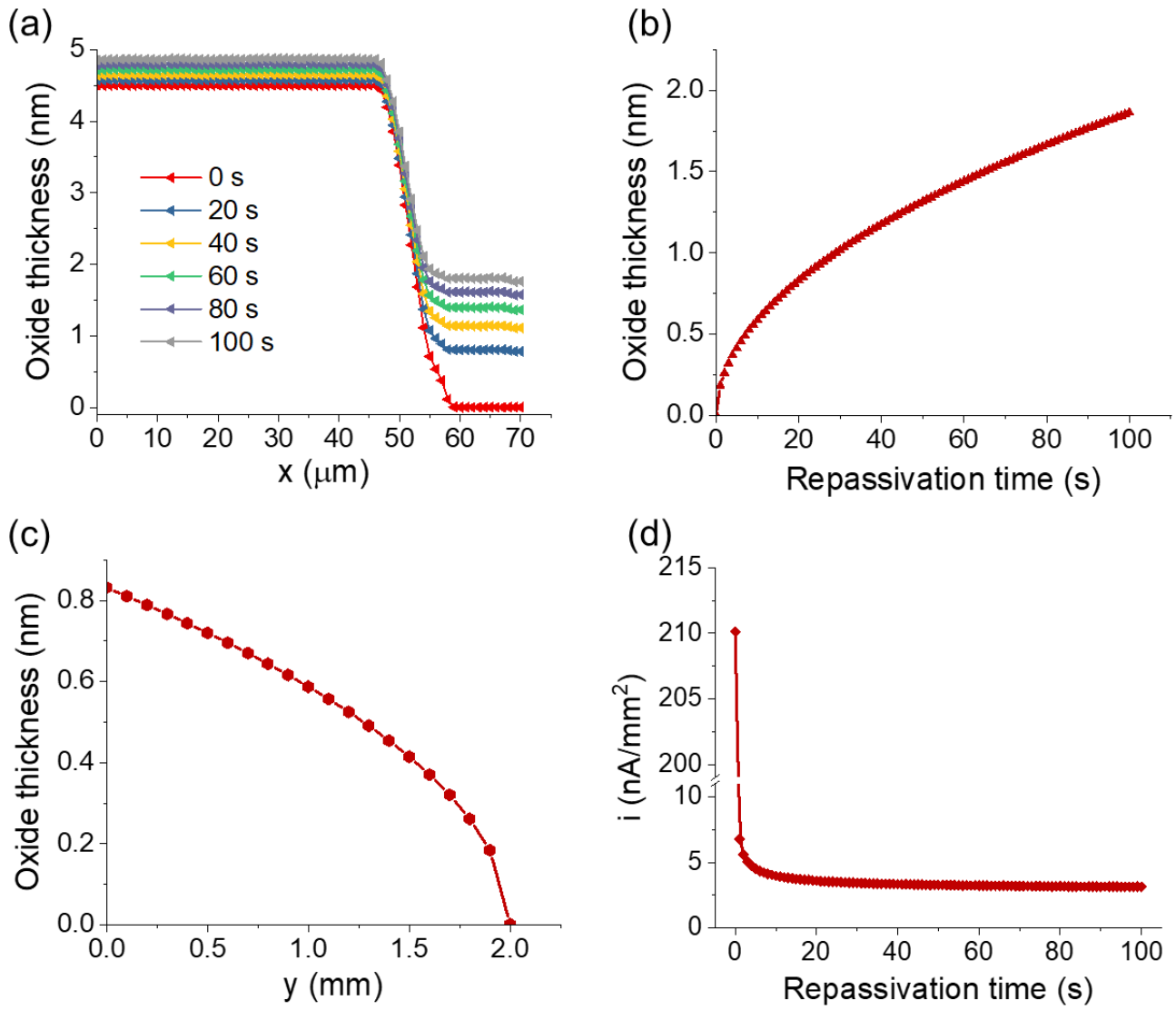

Figure 13. (a) Oxide thickness distribution along the x-axis (TD) as a function of time (0 – 100 sec). (b) Oxide thickness at the bottom of the wear track with respect to repassivation time. (c) Oxide thickness distribution along the y-axis (SD). (d) Current (i) with respect to repassivation time.

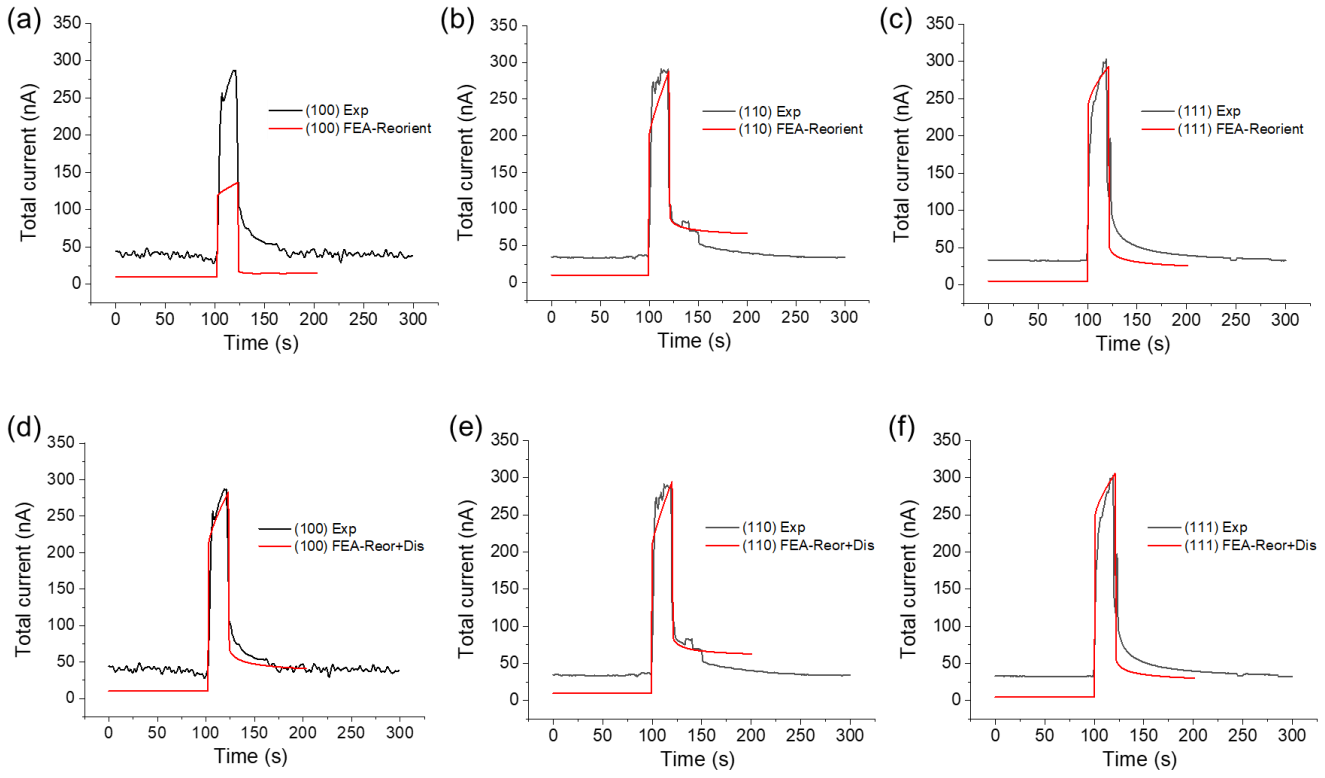

Figure 14. Comparison of experimental measured vs. FE simulated total tribocorrosion current for all samples by considering (a-c) only the lattice reorientation effect, and (d-f) both lattice reorientation and subsurface dislocation effects.

Supplemental Materials

1. Simulation of the indentation test

1.1. Geometry and meshing

The simulation of indentation test was run using an axisymmetric 2D model. The geometry and meshing of the model are plotted in **Fig. S1**. The tip of the indenter was rounded with a radius of 5 μm to prevent the existence of singularity point as well as emulating the actual geometry of the tip.

A maximum meshing size of 25 μm was assigned to the top of the indenter and the sample region away from the contact area. The meshing size was gradually reduced to 2 μm approaching the tip of the indenter. A square area of 20 μm × 20 μm at the contact area was assigned a finer mesh with a meshing size of 1 μm.

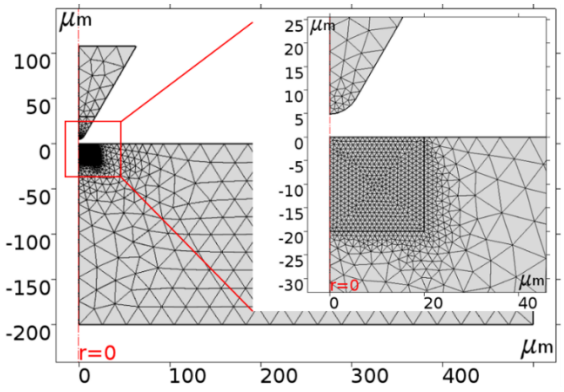

Figure S1. The geometry and meshing of the 2D indentation model with a magnified view at the contact region.

1.1. Governing equations and boundary conditions

The Young's modulus and yield strength used as the inputs for the mechanical properties samples of different orientations was obtained from literatures [36, 38] and listed in **Table 1** of the paper. The indentation was simulated by increasing the displacement of the indenter with a step size of 0.1 μm until the force detected reached 0.1 N. Then the displacement was decreased with the same step size until the force reached zero.

For the material's mechanical behavior, the Hooke's law in cylindrical coordinates and von-Mises yield criterion is applied. For the axisymmetric case, generalized Hooke's law could be expressed as

$$\begin{bmatrix}\sigma_r\\ \sigma_z\\ \sigma_\theta\\ \sigma_{rz}\end{bmatrix} = D\left(\begin{bmatrix}\varepsilon_r\\ \varepsilon_z\\ \varepsilon_\theta\\ \varepsilon_{rz}\end{bmatrix} - \begin{bmatrix}\varepsilon_r\\ \varepsilon_z\\ \varepsilon_\theta\\ \varepsilon_{rz}\end{bmatrix}_{inel}\right), \tag{S1}$$

where D is the elasticity tensor expressed as

$$D = \frac{E}{(1+\nu)(1-2\nu)}\begin{pmatrix}1-\nu & \nu & \nu & 0\\ \nu & 1-\nu & \nu & 0\\ \nu & \nu & 1-\nu & 0\\ 0 & 0 & 0 & \frac{1-2\nu}{2}\end{pmatrix}. \tag{S2}$$

The von-Mises criterion could be expressed as

$$\sqrt{\frac{1}{2}((\sigma_r-\sigma_\theta)^2+(\sigma_r-\sigma_z)^2+(\sigma_\theta-\sigma_z)^2)}-\sigma_y = 0, \tag{S3}$$

where σ_y is the von-Mises yield strength.

1.2. Indentation simulation results

Fig. S2 (a-c) demonstrates the von Mises stress distribution at the highest load predicted by the simulation and (d-f) demonstrates the plastic strain left inside the samples after the indenter was removed. **Fig. S2 (g)** plots the simulated load-displacement curves, which were found to agree well with the experimental results. This proves the validity of the mechanical parameters used in the indentation simulations.

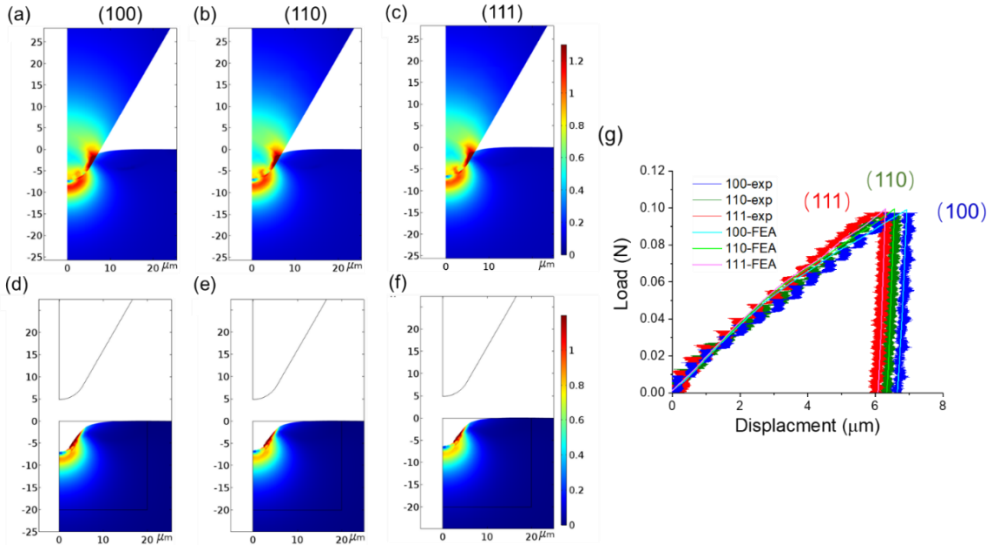

Figure S2. (a-c) Stress distribution at max load (0.1N) for different samples. (d-f) Plastic strain left inside the samples after unloading. (g) The load-displacement curve obtained from simulation in comparison with experiments.

2. Additional Characterization and Corrosion Results

2.1. EDS characterization of the sample surface prior to tribocorrosion test

Energy-dispersive X-ray spectroscopy (EDS) were carried out prior to the tribocorrosion test for polished samples evaluate where there was any residual silica suspension on the surfaces of the samples from the last polishing cycle, which could affect the tribological and corrosion behavior of the samples. **Fig. S3** shows the representative EDS results of the as-polished (100) Al obtained at an accelerating voltage of 5kV. The result shows the existence of Al and minor O from the passive layer, and no trace of Si, which should have a peak at ~ 1.74 keV if exists. This indicates that there is no measurable colloidal silica on the surface of the sample, hence negligible in the later tests and simulations.

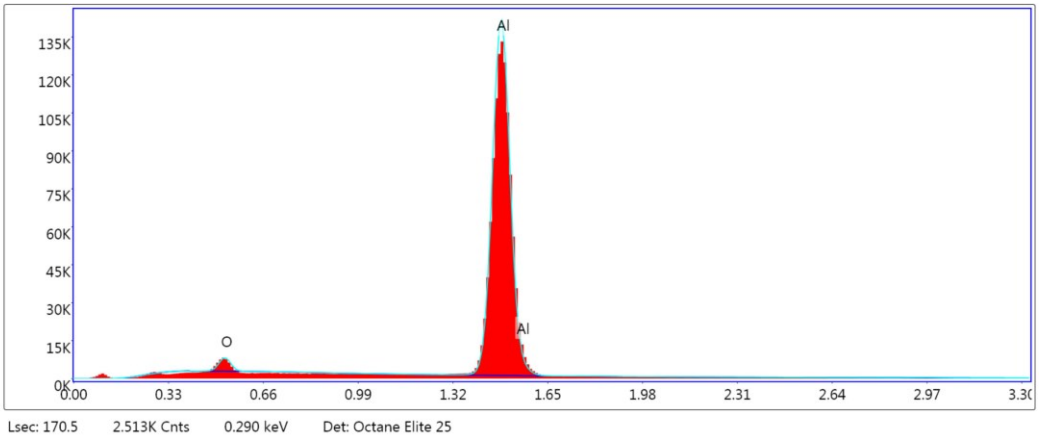

Figure S3. EDS spectra of as-polished (100) Al sample an accelerating voltage of 5 kV.

2.2. PD test and EBSD results of a low symmetry single crystal sample.

In addition to the three high symmetry (i.e. low index) orientations, a low symmetry orientation is prepared from Al single crystal, whose orientation index is determined to be (921) by orientation mapping and inverse pole figure (IPF), as shown in Fig. S4(b) and (c) respectively. The sample polishing and EBSD characterization procedure is the same as those described previously in Section 2.1 and 2.2. The Euler angle of this sample is around (358.4°, 85.5°, 70.3°). The PD results shows that its cathodic reaction kinetics is not linear, hence a Tafel extrapolation of corrosion current is not possible. Nonetheless, the pitting corrosion of (921) is similar to that of (110), and both the cathodic and anodic branch of its PD curve lies in between (100) and (110) orientations, which are indeed the two close by orientations in the IPF. Based on these preliminary results, we believe that the prediction using the linear intercept method

is a good approximation. Nonetheless, the above observations do not rule out the possibility that there could be orientations don't obey this rule. More low symmetry orientations should be studied to cover a wider range of the orientation space to further evaluate this hypothesis in the future.

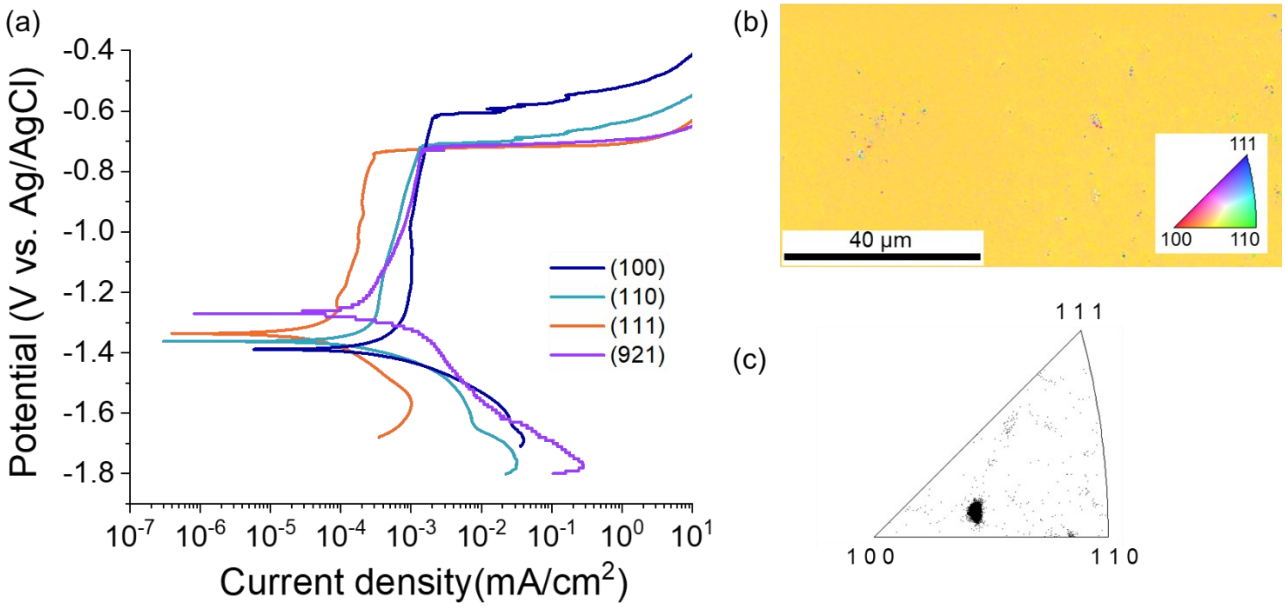

Figure S4. (a) Potentiodynamic polarization curves of (100), (110), (111), and (921) Al single crystal samples in 0.6 M NaCl aqueous solution. (b) Orientation map in sample normal direction, and (c) IPF of the sample normal direction of (921) single crystal, whose Euler angle is around (358.4°, 85.5°, 70.3°).